IEEE Access
Multidisciplinary | Rapid Review | Open Access Journal

Received December 17, 2019, accepted January 1, 2020, date of publication January 10, 2020, date of current version January 21, 2020.

Digital Object Identifier 10.1109/ACCESS.2020.2965594

Sparse Imaging-Based Clutter Suppression and Refocusing of MTs in Passive Bistatic SAR

XIN WANG, (Member, IEEE), AND XIAOZONG SONG
Department of Communication Engineering, Nanjing University of Posts and Telecommunications, Nanjing 210003, China
Corresponding author: Xin Wang (wangx@njupt.edu.cn)

This work was supported by the National Natural Science Foundation of China under Grant 61801232 and Grant 61771182.

ABSTRACT A sparse-imaging-based methodology for the clutter suppression and refocusing of multiple slow-moving targets (MT) in passive bistatic synthetic aperture radar (SAR) is proposed in this paper. The defocused regions of MTs in the bistatic imagery are utilized here. A joint radar projection operator for the static and moving objects is formulated and employed to construct a source separation problem. The Lp norm and square difference maximization constraint are utilized to promote the separation of MT data and the suppression of clutter. After the joint sparse processing, static-scene imagery and MT imagery can be derived simultaneously. Finally, numerical simulations can verify the validity of the proposed methodology.

INDEX TERMS Passive SAR, moving target, clutter suppression.

I. INTRODUCTION

In passive bistatic synthetic aperture radar (SAR), the external illuminator might be static or moving during the data collection integral time and the receiver is placed on a separate platform. As a result of the separation of transmitter and receiver, the passive system has the advantages of good concealing performance, flexible and convenient use, as discussed in [1]–[3]. For the same reason, the clutter nonstationary [4]–[6] is increased and will degrade the performance of traditional suppression methods. The complexity of clutter suppression and imaging processing for moving targets (MT) will also be increased severely [7], [8].

To realize MT imaging processing in passive bistatic SAR, essential clutter suppression and MT data separation are critical since radar data is mix-received. When the Doppler frequencies of MTs are discriminative from the clutter, filtering operation can be performed to extract MT data directly. Many scholars proposed to implement MT refocusing based on the extracted defocused regions of interest (ROI). The analytical expressions of the phase error terms of MTs are derived in reference [9]–[11]. Then, refocusing operation is implemented via phase error compensation and Fourier transform. Some autofocus-based methods [12], [13] have also been discussed to realize MT refocusing by searching for moving parameters in a predefined region. The focal qualities of the derived imageries are evaluated to find the best result. Whereas filtering operation generally cannot remove the energy of clutter and static targets completely, especially when MTs located inside strong clutter regions. Besides, these algorithms cannot be applied for multiple MTs imaging simultaneously, and the computational burden is generally severe.

However, it is more common that MTs locate inside strong clutter regions. The displaced phase center antenna (DPCA) [14], space-time adaptive processing (STAP) [15] and along-track interferometry (ATI) [16] algorithms have been developed to suppress clutter in this case. An over-completed velocity dictionary and a Doppler dictionary are then constructed to realize multiple MTs refocusing [17], [18], respectively. However, these algorithms are generally derived for multi-channel monostatic SAR data. The DPCA and STAP processing have been extended to bistatic cases [19], [20], respectively. Nevertheless, the non-stationary characteristic and severe range dependence of clutter, which is introduced by the bistatic collection geometry, will degrade the performances of these algorithms. Several methods are considered to restore the performance of STAP by using some prior information of the data collection geometry or aligning the dominant clutter subspaces of each range [21], [22]. Moreover, the Doppler-DPCA and ATI are also discussed to suppress the clutter in reference [23]. However, these methods generally are not suitable for the single-channel data, and the performance is closely related to the bistatic data collection geometry.

The associate editor coordinating the review of this manuscript and approving it for publication was Ivan Lee.

To implement the MTs refocusing processing in one channel passive SAR, we propose a joint sparse-based method in this paper. The sparse constraint has also been utilized in compressed sensing (CS) [24], [25] to realize SAR/ISAR imaging, tomography, and ground moving target indication in the past decades. The CS theory can implement the complete recovery of the original signal with fewer measurements and thus is very useful when the data is under-sampling or a part is missing. In reference [26], the CS theory is discussed to reconstruct the imagery with very few sampling data. Then, Hu et al. investigate a series of CS-based algorithms from different aspects [27]–[29] to implement high-resolution imaging based on sparse apertures or random down-sampling data.

Given the above attractive and successful application experiences, we try to use the same sparse constraint in CS to realize the suppression of clutter and separation of MT data in this paper. The Doppler phase history differences between MT signal and clutter data, which were used for moving objects detection [30], [31], are utilized in this paper to separate MT data from the mixed imagery. A joint projection operator is formulated instead of using an over-complete Doppler or velocity dictionary. The MT data separation from the smeared SAR imagery is thus converted to be a sparse-based optimization problem. After the joint sparse-based refocusing, MT imagery and static scene imagery could be derived. The general SAR data collection geometry and signal model are described in Section II firstly. Then, the joint sparse imaging methodology is presented and discussed in Section III. Finally, numerical simulation verifies that the algorithm can implement multiple moving target imaging conveniently.

II. PASSIVE BISTATIC SAR SIGNAL MODEL

Fig. 1 depicts the passive bistatic SAR data collection geometry, where the scene center is defined as the origin of the coordinate system. The external illuminator is stationary during the data collection interval while the receiver platform flights along y axis with a constant velocity v_r and the altitude h_r. The coordinates of transmitter and receiver at aperture center time are defined as (x_{tc}, y_{tc}) and (x_{rc}, y_{rc}), respectively.

We assume that the illuminated scene is static and multiple MTs located at (x_m, y_m) move with constant velocities during the data collection interval. The received passive SAR data is thus a mixture of clutter and the electromagnetic wave reflected from MTs. After range compression, the passive SAR data can be expressed as

$$\begin{aligned} &S_r(k_r, t) \\ &= \sum_s w_r(f_r)\, w_a(t - t_c) \exp\left[-j2\pi \frac{(f_r + f_c)}{c} R_s(t)\right] \\ &\quad + \sum_m w_r(f_r)\, w_a(t - t_c) \exp\left[-j2\pi \frac{(f_r + f_c)}{c} R_m(t)\right], \end{aligned} \tag{1}$$

where the operator $\sum \cdot$ indicates the coherent addition of the signal from all the illuminated targets, t is the azimuth

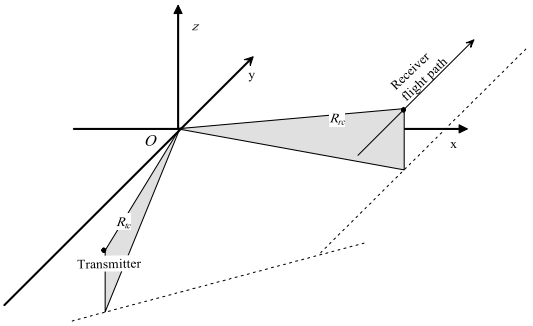

FIGURE 1. Passive SAR data collection geometry with one static transmitter.

(slow) time centered at t_c, f_r is the range frequency, f_c denotes the center frequency, and c is the speed of light. In Eq. (1), the function $w_r(\cdot)$ is the range envelope, $w_a(\cdot)$ is the azimuth envelope determined by the composite antenna pattern, and $R_s(\cdot)$ and $R_m(\cdot)$ are referred to as the instantaneous bistatic slant ranges of the static target and MTs. Herein, without loss of generality, we define the azimuth center time $t_c = 0$.

Since the transmitter is stationary, the Doppler phase history of the static targets is only determined by their coordinates and the flight path of the receiver. Performing Taylor expanding on the phase term in (1), we can derive the Doppler center frequency f_{ac} and modulation rate k_a in the phase history domain as

$$f_{ac} = \frac{v_r}{\lambda} \frac{(y_{rc} - y_s)}{R_{sr}(t_c)}, \tag{2a}$$

$$k_a = \frac{1}{\lambda}\left[\frac{v_r^2}{R_{sr}(t_c)} - \frac{v_r^2 (y_{rc} - y_s)^2}{R_{sr}^3(t_c)}\right], \tag{2b}$$

where $R_{sr}(t_c)$ is the slant range from the targets (x_s, y_s) to the receiver aperture center. Due to the motion of MTs, the Doppler parameters of themselves become

$$\begin{aligned} f'_{dc} = \frac{1}{\lambda}\Bigg[&\frac{(x_{rc} - x_m)v_{xm} - (y_{rc} - y_m)\left(v_r - v_{ym}\right)}{R_{mr}(t_c)} \\ &+ \frac{(x_{tc} - x_m)v_{xm} - (y_{tc} - y_m)v_{ym}}{R_{mt}(t_c)}\Bigg], \end{aligned} \tag{3a}$$

$$\begin{aligned} k'_a = \frac{1}{\lambda}\Bigg\{&\frac{v_{xm}^2 + \left(v_r - v_{ym}\right)^2}{R_{mr}(t_c)} + \frac{v_{xm}^2 + v_{ym}^2}{R_{mt}(t_c)} \\ &- \frac{\left[(v_r - v_{ym})(y_{rc} - y_m) - v_{xm}(x_{rc} - x_m)\right]^2}{R_{mr}^3(t_c)} \\ &- \frac{\left[v_{ym}(y_{rc} - y_m) + v_{xm}(x_{rc} - x_m)\right]^2}{R_{mt}^3(t_c)}\Bigg\}, \end{aligned} \tag{3b}$$

where, $R_{mr}(t_c)$ and $R_{mt}(t_c)$ are referred to as the slant ranges of the MT to the receiver and the transmitter at aperture center time, respectively, v_{xm} and v_{ym} are the velocities of MTs along x and y axes, and λ denotes the wavelength. For convenience, the subscript s and m in the following discussion all correspond to the static scene and MTs. It can be seen from Eq. (2) and Eq. (3) that the Doppler characteristics of static

targets and MTs are generally discriminative. So, the phase compensation filters in traditional imaging algorithms, which are designed by assuming the illuminated targets are stationary, are commonly mismatched for MTs data. Thus, smearing and geometry distortion will generate in the derived SAR imagery.

III. SEPARATION AND REFOCUSING OF MTs IMAGERY

In consideration of the discriminative Doppler characteristics of clutter and MTs data, we try to separate the bistatic imagery by projecting it on different radar system matrixes. The clutter suppression and MTs separation are thus converted to a sparse-based source separation problem. Then, the back data from MTs can be reconstructed and refocused with a significantly decreased signal to clutter ratio (SCR). The detailed processing flow will be described in the following discussion.

A. PROPOSED OPTIMIZATION PROBLEM

Based on the equation in Eq. (1), a joint bistatic radar projection operator is formulated as $\mathrm{F}_r = [\mathrm{F}_s, \mathrm{F}_m]$. The matrixes $\mathrm{F}_s \in \mathbb{C}^{\mathrm{N}_I \times \mathrm{N}_I}$ and $\mathrm{F}_m \in \mathbb{C}^{\mathrm{N}_I \times \mathrm{N}_I}$ are denoted as the imaging projection operators of static scene and MTs, and the notation N_I is referred to as the length of MT imagery. In the matrix F_s, the column vector is a composite vector obtained by stacking the system function from one static target and one MT. Using the composite matrix F_r, the bistatic scene imagery and MT imagery can be obtained after as

$$\mathrm{S} = \mathrm{F}f + \mathrm{n}_I, \tag{4}$$

where,

$$\mathrm{F} = \mathrm{F}_r^H \mathrm{F}_r,$$

In Eq. (4), $\mathrm{S} \in \mathbb{C}^{2\mathrm{N}_I \times 1}$ is derived by stacking the bistatic SAR imagery reconstructed via the joint radar projection operator F_r, $f = [f_s, f_m]^T \in \mathbb{C}^{2\mathrm{N}_I \times 1}$ is a composite column vector composed of the radar field information of clutter and MTs, the superscript H indicates the conjugate transpose of a matrix, and the notation n_I is referred to as the noise vector.

Generally, the expression of F_s is deterministic since it is only related to SAR system parameters and back-projection pixel coordinates. By contrast, the MT radar projector F_m is difficult to formulate as it needs an accurate estimation of the Doppler parameters of MTs. In this case, there is no closet analytical solution of Eq. (4). The sparse-based optimization method could be employed to help find the solution and realize the separation of clutter. After denoting the reconstructed imagery as the sparse representation of one over-completed dictionary D, we formulate the following optimization function as,

$$\min_{\alpha, \mathrm{F}_m} J_0(\alpha, \mathrm{F}_m) = \min_{\alpha, \mathrm{F}_m} \|\mathrm{S} - \mathrm{FD}\alpha\|_2^2 + \lambda_1 \|\alpha\|_p^p, \tag{5}$$

where $\|\cdot\|_p^p$ denotes ℓ_p norm, λ_1 is a positive scaling parameter, $\alpha = [\alpha_s, \alpha_m]^T$ is the sparse coefficient of the imagery. In Eq. (5), only the sparse coefficient α and MT radar projector F_m are unknown and needed to be updated in the iterative computation. The first term is a data fidelity term, which incorporates the joint SAR observation model in Eq. (4) and the RCS information of the illuminated targets. The second term aims to constrain the solution to be sparse. Moreover, the dictionary D could be designed as a fixed wavelet or DCT dictionary. We do not discuss the combination and training of the dictionary as it is beyond the research scope of this paper.

B. DATA SEPARATION BY USING LP NORM

Generally, the ℓ_p norm with $p = 0$ is selected to constrain the solution to be sparse. Greedy methodologies [23] and the ℓ_1 relaxation method have been developed to solve this problem approximately. Whereas the accuracy of these methods will degrade when the initialized MT radar projection operator is mismatched. As discussed in reference [28], [29], the ℓ_p norm with $0 < p < 1$ will result in a more sparse solution in comparison and thus is used in our method.

The utilization of ℓ_p norm is viewed as imposing an energy-type constraint on the solution in reference [28]. From a statistical point of view, this would be equivalent to assume a prior model on the coefficients α. Herein, we use it to suppress artifacts and increase the resolvability of scatters in the solution. By solving the optimization problem in Eq. (5), the mixed imagery will be projected on the system operators F_s and F_m, respectively. The extraction of MT signals is thus converted as a source separation operation. As the coherence of clutter and MTs signal to the two system operators are distinct, the energy of them will be separated with different signal to noise ratio (SNR). Since F_m is mismatched for clutter, the static targets will be focused in the vector f_s and smeared in MT vector f_m. These smeared impulse response functions are viewed as artifacts and generally can be suppressed by using the sparse constraint. After several iteration computations, most of the energy of the static scene will thus be concentrated on f_s and removed from f_m. The separated static-scene imagery and MTs imagery will finally be obtained simultaneously.

However, the differences between the Doppler phase histories of the static scene and MTs sometimes are not so large and a few cross-projection coefficients might still exist after using the sparse constraint. It is normal as the two radar projection operators are not orthogonal or severely discriminative. In this case, the separation results might not be satisfactory. To limit the energy of the cross-projection, we modify the cost function in Eq. (5) as

$$\min_{\alpha, \mathrm{F}_m} J(\alpha, \mathrm{F}_m) = \min_{\alpha, \mathrm{F}_m} \|\mathrm{S} - \mathrm{FD}\alpha\|_2^2 + \lambda_1 \|\alpha\|_p^p - \lambda_2 \|\mathrm{D}\alpha - \mathrm{F}_d \mathrm{D}\alpha\|_2^2 \tag{6}$$

where

$$\mathrm{F}_d = \begin{bmatrix} \mathrm{I}, & \mathrm{F}_m^H \mathrm{F}_s \\ \mathrm{F}_s^H \mathrm{F}_m, & \mathrm{I} \end{bmatrix}$$

In Eq. (6), the matrix F_d originates from the cross-projection components in the matrix $\mathrm{F}^H\mathrm{F}$, λ_2 is a positive parameter for the cross-projection suppression, and $\mathrm{I} \in \mathbb{C}^{\mathrm{N}_I \times \mathrm{N}_I}$ is an

identity matrix. The third term in Eq. (6) aims to maximize the sum of squared differences of clutter and MTs imageries. Based on these constraints, the bistatic imagery could be separated after several iterations.

C. ITERATIVE SOLUTION

The iterative computation of Eq. (6) can be divided into two sub-problems. First, updating α by fixing F_m and then updating F_m by fixing α. The two procedures are iteratively implemented until the derived results converge.

1) THE SPARSE COEFFICIENT UPDATE

Since the ℓ_p norm is non-differentiable around the origin, an exact solution of Eq. (6) is difficult to obtain directly. As discussed in reference [28], the following approximation expression is applied instead of ℓ_p norm

$$\|\mathrm{z}\|_p^p \approx \sum_{i=1}^{N_z} \left(|z(i)|^2 + \varepsilon\right)^{p/2}, \tag{7}$$

where $\varepsilon \geq 0$ is a small positive constant, N_z denotes the length of the vector z, $z(i)$ is referred to as the ith element in z. Substituting Eq. (7) into the cost function in Eq. (6), a modified equation is given as

$$J_m(\alpha, \mathrm{F}_m) = \|\mathrm{S} - \mathrm{FD}\alpha\|_2^2 + \lambda_1 \sum_{i=1}^{2N_I} \left(|\alpha(i)|^2 + \varepsilon\right)^{p/2} - \lambda_2 \|\mathrm{D}\alpha - \mathrm{F}_d \mathrm{D}\alpha\|_2^2, \tag{8}$$

The modified cost function $J_m(\alpha, \mathrm{F}_m)$ will always close to $J(\alpha, \mathrm{F}_m)$ when $\varepsilon \to 0$. There is no closed-form solution for the minimization of Eq. (8) and the quasi-Newton methods might be used to derive the solution as discussed in reference [29].

Calculating the gradient of Eq. (8) to α, we can obtain the following iterative formula based on the Hessian matrix approximation [29]

$$\left[\mathrm{H}\left(\widehat{\alpha}^{(n)}\right)\right]\widehat{\alpha}^{(n+1)} = (1-\gamma)\left[\mathrm{H}\left(\widehat{\alpha}^{(n)}\right)\right]\widehat{\alpha}^{(n)} + 2\gamma \mathrm{F}^H \mathrm{S}, \tag{9}$$

where

$$\begin{aligned}\mathrm{H}\left(\widehat{\alpha}^{(n)}\right) \triangleq\ & 2\mathrm{D}^{\mathrm{H}}\mathrm{FD} \\ & + p\lambda_1 diag\left\{\left(\left|\widehat{\alpha}^{(n)}(j)\right|^2 + \varepsilon\right)^{p/2-1}\right\}, \\ & - \lambda_2 \left[(\mathrm{I} - \mathrm{F}_d)\,\mathrm{D}\right]^H (\mathrm{I} - \mathrm{F}_d)\,\mathrm{D}\end{aligned} \tag{10}$$

In Eq. (9), γ denotes the iteration step, $\widehat{\alpha}^{(n)}$ is the estimation result after the nth iteration. Eq. (10) is a linear equation with conjugate matrix coefficients. The sparsity of $\mathrm{H}\left(\widehat{\alpha}^{(n)}\right)$ is increased by neglecting the elements in $\mathrm{F}^H\mathrm{F}$ whose magnitudes are smaller than 1% of the largest element. Hence, the conjugate gradient method could be applied to search for the solution of Eq. (8). However, we find that the second term in Eq. (10) sometimes might amplify the small values in the solution and thus affect the convergence rate. To solve this problem, we employ the conjugate gradient hard threshold method here, which has been proposed in reference [32] to solve for data recovery problem. The threshold function is applied to the derived solution $\widehat{\alpha}^{(n)}$ to accelerate the convergence rate. Finally, the vector $\widehat{f}^{(n)} = D\widehat{\alpha}^{(n)}$ can be restacked to obtain the static scene and refocused MT imageries simultaneously.

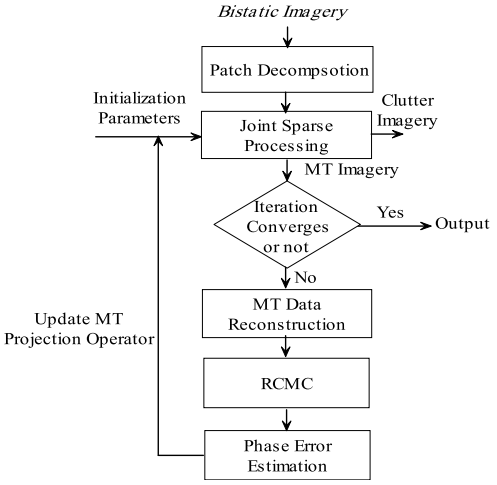

FIGURE 2. Joint sparse-based processing flow.

2) MT RADAR PROJECTION OPERATOR UPDATE

Another factor that affects the separation of MTs imagery is the designing of radar operator F_m. In practical data processing, the initialized $\widehat{\mathrm{F}}_m^0$ could be formulated based on some prior information or the estimation results of moving parameters. When the mismatched phase error of $\widehat{\mathrm{F}}_m^0$ is not too large, static-scene imagery and MT imagery could be separated and derived directly. Otherwise, the residual energy of clutter might still exist in the reconstructed MT imagery. To avoid this problem, we try to update the operator F_m during the iterative computation interval until the solution converges. In this case, the optimization problem becomes as

$$\min_{\mathrm{F}_m} \left\| \mathrm{S} - \begin{bmatrix} \mathrm{F}_s^H \mathrm{F}_s \mathrm{D}\widehat{\alpha}_s^{(n)} + \mathrm{F}_s^H \mathrm{F}_m D\widehat{\alpha}_m^{(n)} \\ \mathrm{F}_m^H \mathrm{F}_s D\widehat{\alpha}_s^{(n)} + \mathrm{F}_m^H \mathrm{F}_m \mathrm{D}\widehat{\alpha}_m^{(n)} \end{bmatrix} \right\|_2^2 \tag{11}$$

As no additional constraint is performed on F_m, the direct solution of Eq. (11) is difficult to obtain. In reference [12], [13], the MT parameters are updated by search in a predefined region based on the maximization of imagery sharpness or entropy. However, this method is computationally expensive and cannot cope with multiple MTs with different velocities.

In the iterative computation, the complex matrix product is denoted as the multiplications of real value matrixes. The sparse constraint is employed on the coefficient of the ampli-

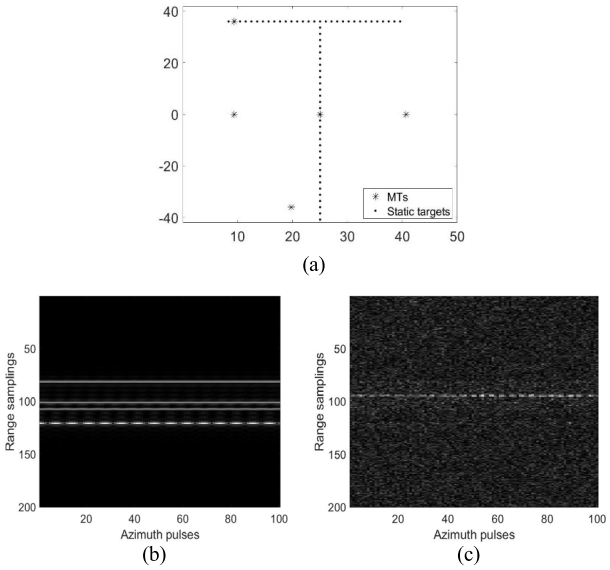

FIGURE 3. The simulated MTs and SAR data. (a) The geometry relationship of MTs; (b) The range compressed MT data; (c) The range compressed radar data combined with clutter and noise.

TABLE 1. System simulation parameters.

Symbol	Transmitter	Receiver
Velocity	0m/s	250m/s
Range	1000m	7000m
Bandwidth	100MHz	
PRF	1000Hz	

TABLE 2. Moving parameters.

Symbol	MT1	MT2	MT3	MT4	MT5
Azimuth position	10	25	40	5	10
Range position	20	20	20	20	35
v_{xm}	1.8m/s	1.8m/s	1.8m/s	1.8m/s	1.8m/s
v_{ym}	2m/s	2m/s	2m/s	2.5m/s	3m/s
SCR	-2.3dB	-2dB	0dB	-2dB	-5dB

tude information of f. The phase information of the imagery is thus not maintained after the iterative deduction. Herein, we design to reconstruct the complex MT patch data as

$$\widehat{\mathrm{Y}}_m^{(n+1)} = \widehat{\mathrm{F}}_m^{(n)} \left[\left| \widehat{f}_m^{(n)} \right| \odot \exp\left(\angle \widehat{f}_m^{(0)} \right) \right], \tag{12}$$

where, $\odot$ denotes an elementwise product operation, $|\cdot|$ and $\angle\cdot$ indicate the computation of amplitude and angle of a vector, $\widehat{f}_m^{(n)}$ and $\widehat{f}_m^{(0)}$ are referred to as the constructed and initialized MT imagery, respectively. Though the MT system operator $\widehat{\mathrm{F}}_m^{(n)}$ might deviate from the real values, most of the clutter energy is still suppressed in the derived sparse MT imagery. Compared with the original SAR data, the SCR in the reconstructed MT data $\widehat{\mathrm{Y}}_m$ will be decreased significantly.

Clearly, parameter estimation operation could be performed on the reconstructed MT data $\widehat{\mathrm{Y}}_m$ directly to update the system function. The time-frequency analysis and interferometry processing methodologies have been developed for moving parameter estimation in one channel SAR. However, the existence of the range cell migration (RCM), generally will degrade the performance of these methods. Many methodologies [33], [34] have been proposed for range cell migration cell (RCMC) based on one-order or two-order Keystone transforms. Herein, the fractional Fourier transform is used to estimate the residual RCM and phase error. The radar projection operator is updated as $\widehat{\mathrm{F}}_m^{(n+1)} = \widehat{\mathrm{F}}_{er}^{(n)} \odot \widehat{\mathrm{F}}_m^{(n)}$, where $\widehat{\mathrm{F}}_{er}^{(n)}$ is formulated based on the time-frequency analysis results. The ith column vector of $\widehat{\mathrm{F}}_m^{(n+1)}$ is derived via stacking the Doppler phase history data of MTs in $f_m(i)$, which is space-variant and related to the positions of the pixel $f_m(i)$. Using this matrix structure, we can formulate the Doppler data vectors of MTs according to their locations in the imagery and do not need to compute multiple projection operators when MTs move with different velocities. Then, the subsequent iterative processing could be carried continually until the solution converges. The detailed iteration processing is listed in Algorithm 1.

Algorithm 1 Joint Sparse-Based Clutter Suppression and MT Refocusing

1. Input: Defocused MT imagery patches;
2. Initialization: $\widehat{f}^{(0)}$, $\widehat{\mathrm{F}}_m^{(0)}$, F, λ_1, λ_2, p;
3. While not converge do
4. Update the reconstructed result $\widehat{\alpha}^{(n+1)}$ according to Eq. (9);
5. Update the MT projection operator $\widehat{\mathrm{F}}_m^{(n+1)}$ according to the parameter estimation results;
6. End
7. Output: Static scene imagery and MT imagery.

IV. PATCH DECOMPOSITION

The huge dimension of SAR real data and imagery for the illuminated scene will increase the complexity of our method and limit the application. As the defocused area of MTs is usually distributed in small patches of SAR imagery, we do not need to construct the radar projection operator of the whole scene. Patch processing is introduced and employed in the proposed method to reduce the computational burden.

The defocused MT patches in SAR imagery is extracted firstly as the input of iterative computation. Then, the SAR joint imaging operator F corresponding to the imagery patches is formulated and utilized. The number of multiplication operations in the computation of F is proportional to

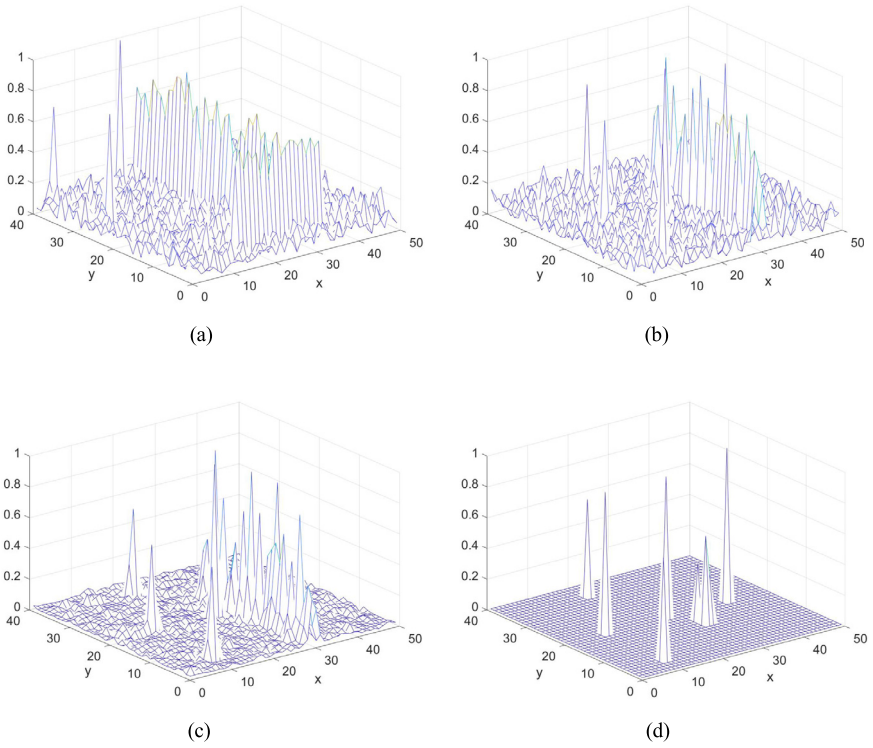

FIGURE 4. Comparison of the 3-D imaging results. (a) Original bistatic imagery; (b) Refocused MT imagery via matched filtering; (c) Interferometry result; (d) MT imagery derived via our method.

the dimension of SAR data and patch imagery. To further reduce the computational cost, we employ an azimuth down-sampling operation when reconstructing the radar projection operators and MT data $\widehat{Y}_m^{(n+1)}$. In iteration processing, a conjugate gradient hard threshold algorithm with high convergence speed is used and the computational burden is proportional to the length of the sparse coefficient of SAR imagery vector. As a result of the utilization of sub patch processing and azimuth down-sampling, the computational cost in joint sparse MT imaging will be decreased significantly.

In practical data processing, the size of one MT patch is generally very small (the patch size for one MT might be restricted as 30×30 in low resolution case) and the number of iteration computation is less than 10 when the derived solution converges. Moreover, as the dimensions of the SAR imagery patches are very small, the computation of F can be implemented approximately, in which the value of the elements $\mathrm{F}(i, j)$ with $|i - j| = m$ is the same. In this case, the total computational burden is much lower than that of autofocus processing of SAR data. In conclusion, the detailed flow of joint sparse imaging processing is depicted in Fig. 2. After iteration converges, the static scene and MT imageries can be derived simultaneously.

V. SIMULATION

Numerical simulations will be performed in this section to prove the validity of the joint sparse-based algorithm. The passive SAR data from 5 ground MTs and 72 static targets in Fig. 3(a) are simulated and then processed via the joint sparse-based processing. The receiver platform flights along y axis with the constant velocity 250m/s while the transmitter is stationary during the data collection interval. The system parameters and MTs velocities are given in Table 1 and Table 2. The bistatic angle is 45° and the polar angle of transmitter is 45°. After range compression, the MTs data and synthesized SAR data are obtained in Fig. 3(b) and Fig. 3(c), respectively. It could be seen from these figures that the received radar data of MTs is masked by the clutter which should be suppressed in advance.

After back-projection processing, the bistatic SAR imageries can be derived in Fig. 4(a) and Fig. 5(a). The SCR values are calculated as the ratio of the energies of MT and clutter in SAR imagery and listed in Table 2. It can be seen from Fig. 4(a) and Fig. 5(a) that the smeared MTs are masked by the strong surrounding clutter. In this case, it is difficult to suppress or separate the clutter to derive the refocused MT imagery with high SCR.

The regularization parameters employed in the simulation are defined as $\lambda_1 = 0.15$, $\lambda_2 = 0.05$, and $p = 0.5$. These parameters are empirical value which are derived from reference [29] and our experience. The bistatic SAR imagery can be used as the initialization $\widehat{f}^{(0)}$. Assuming the estimated velocities of MTs along x and y axes are $v'_{xm} = v_{xm} + \Delta v_{xm}$ and $v'_{ym} = v_{ym} + \Delta v_{ym}$ respectively, an initial estimation of

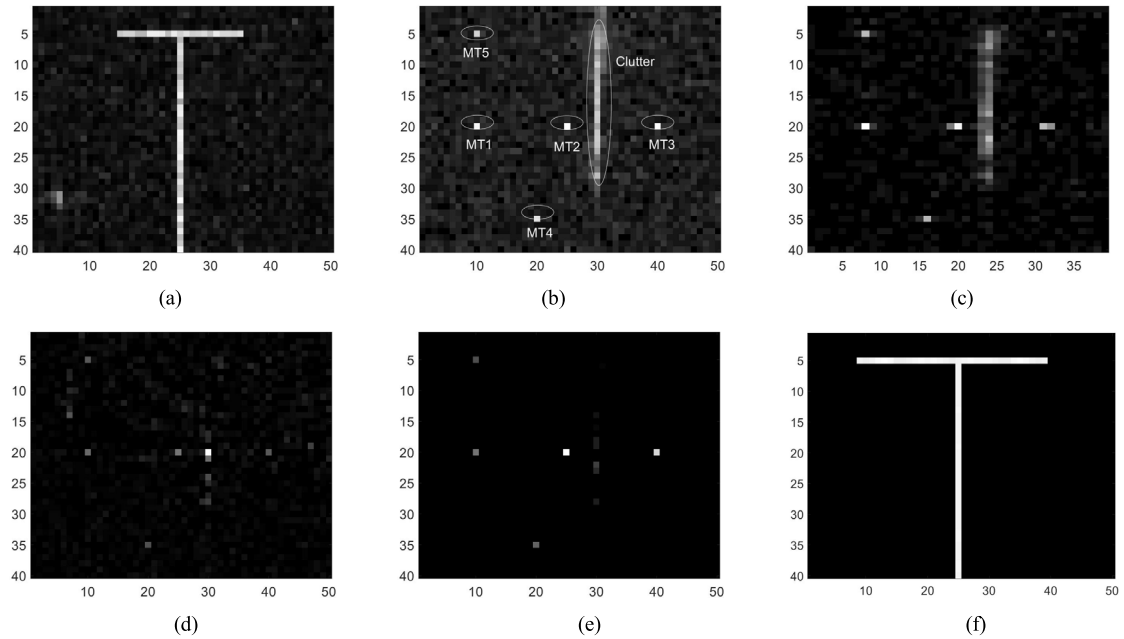

FIGURE 5. MF and sparse imaging result. (a) Original SAR imagery; (b) Refocused imagery derived by frequency domain matched filtering; (c) Imagery result after interferometry; (d)Imagery derived based on ℓ_1 norm regularization; (e) and (f) MT imagery and static scene imagery after the joint sparse processing.

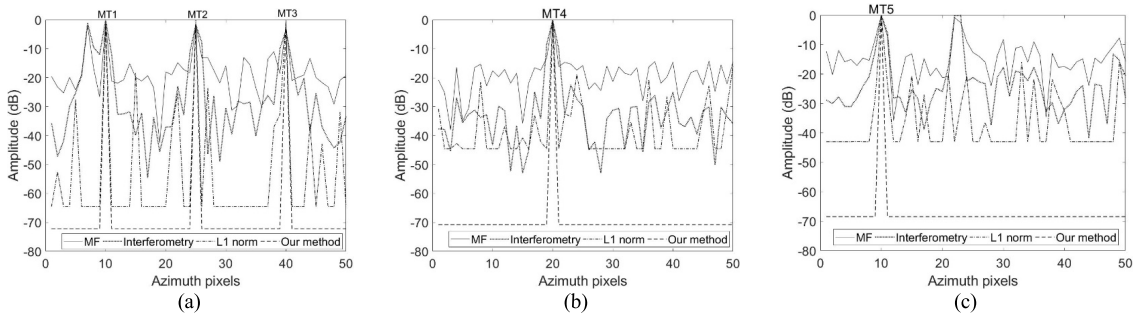

FIGURE 6. Comparison of azimuth profiles of MTs before and after clutter suppression. (a)MT1, MT2 and MT3; (b)MT4; (c) MT5.

the radar MT projection operator $\widehat{\mathrm{F}}_{\mathrm{m}}^{(0)}$ could be constructed. The notations Δv_{xm} and Δv_{ym} are referred to as mismatched velocity errors. In practice, if some prior information about MT is given in advance, a larger velocity could also be selected to start for the first iteration without parameter estimation.

Here, for comparison with our method, the matched filtering, multi-look interferometry, and ℓ_1 norm regularization methods are performed on the defocused MT imagery, respectively, and the results are given in Fig. 5(c), (d) and (e). After using these methods, the clutter is suppressed to some extent but there is still residual energy of the strong static targets, which can be concluded from Fig. 5 (a)-(e). By contrast, the imageries of 5 MTs and 72 static targets are obtained with high quality by using our joint sparse processing and the results are depicted in Fig. 5 (e)-(f).

To further verify our method, the azimuth profiles of the refocused 5 MTs are depicted in Fig. 6 for comparison. It can be seen from Fig. 6 that some residual energy of strong static targets still exists after interferometry and ℓ_1 regularization processing. It is noteworthy that the strong clutter is suppressed significantly after the joint sparse processing as depicted in Fig. 6.

When the initialized parameters deviate from the real values, MT doppler parameter estimation and update should be performed in the iteration computation. Though the initialized MT radar projection operator is mismatched, most of the clutter energy is still suppressed in the derived imagery after the iteration computation, as shown in Fig. 7 (b). The horizontal and vertical axis in Fig. 7(a)-(c) are referred to as the back-projection pixel along x and y axes. MT radar patch data is then reconstructed based on the Eq. (12) and given

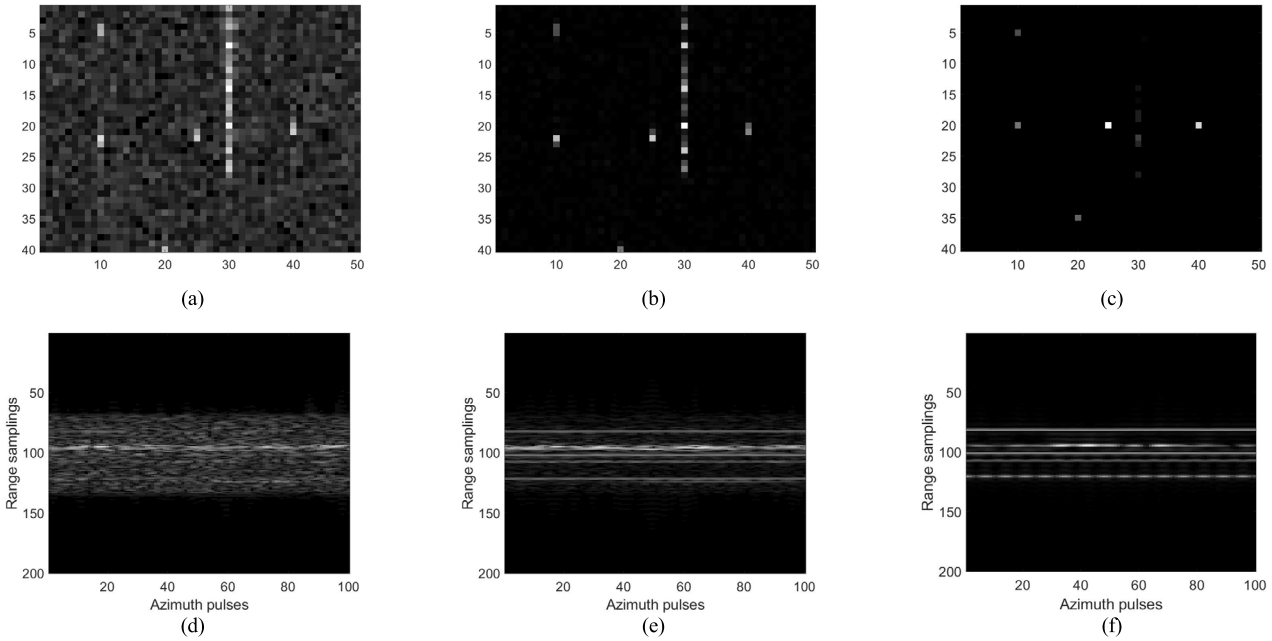

FIGURE 7. MT imagery and the reconstructed MT data. (a) and (d) Initialized MT imagery and radar data; (b) and (e) MT imagery and reconstructed data after the first iteration; (c) and (f) MT result and reconstructed data derived after joint sparse processing.

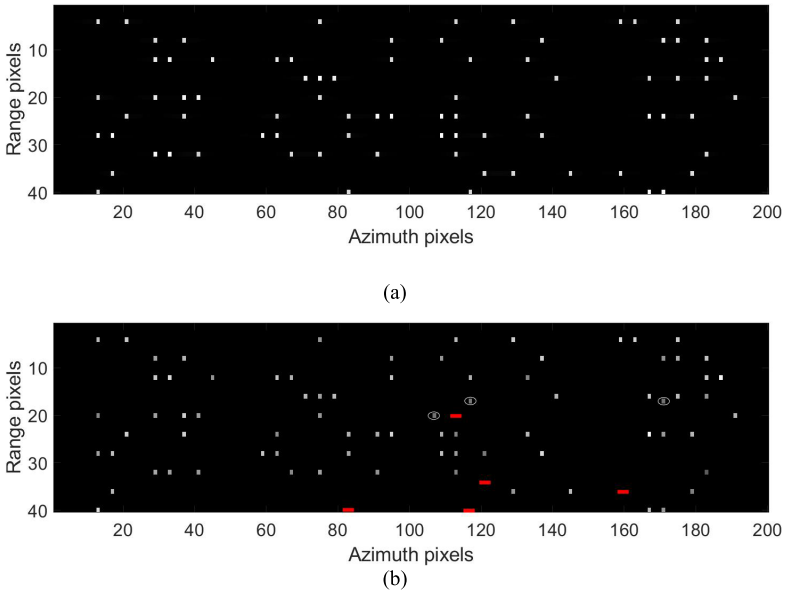

FIGURE 8. Results after the joint sparse-based refocusing. (a) Simulated MTs; (b) Detection results.

in Fig. 7 (e) and (f). It can be concluded that the clutter is suppressed after the first iteration computation. The Doppler parameter estimation operation is then performed after keystone transform and range cell migration correction. After updating the MT system operator based on the estimated parameters, we can finally obtain the MT imagery and radar patch data in Fig. 7(c).

To assess the performance of our algorithm, we synthetic the passive SAR data from 80MTs and a real static scene imagery. Then, the joint sparse-based processing is performed on the synthesized data to derive the refocused MT imagery. The azimuth velocities and SCR values of simulated MTs are given in Table 3. Patch decomposition operation is performed and then sub-imageries are derived and combined. The refocused result is depicted in Fig. 8(b) and given in Table 2, where the false refocused targets are marked by the white ellipse and the missed targets are denoted with the red rectangles. It can be concluded from Fig. 8 and Table 3 that our

TABLE 3. Simulation parameters of MTs.

	Successful refocused	False refocused	Missing targets
0dB-10dB, 5m/s-10m/s	20	0	0
0dB-10dB, 1m/s-5m/s	19	0	1
-10dB-0dB, 5m/s-10m/s	19	2	1
-10dB-0dB, 1m/s-5m/s	20	1	0

algorithm can realize the refocus processing of multiple MTs effectively.

VI. CONCLUSION

A joint clutter suppression and MT refocusing method is proposed in this paper. The defocused ROI in bistatic SAR imagery is utilized in this method. After the joint sparse processing, the mixed imagery is separated to obtain the refocused MT imagery and the static scene imagery, respectively. Numerical simulations verify that the presented methodology can realize the refocusing of multiple MTs effectively. In the joint sparse-based processing, the designing of the regularization parameters does affect the separation of the energy of the static and moving targets. However, this problem is common in sparse-based iterative computation methods. We plan to discuss the influence of the parameter designing on the performance of our algorithm in the future.

REFERENCES

[1] M. Antoniou, Z. Zeng, L. Feifeng, and M. Cherniakov, "Experimental demonstration of passive BSAR imaging using navigation satellites and a fixed receiver," *IEEE Geosci. Remote Sens. Lett.*, vol. 9, no. 3, pp. 477–481, May 2012.
[2] S. Duque, P. Lopez-Dekker, and J. J. Mallorqui, "Single-pass bistatic SAR interferometry using fixed-receiver configurations: Theory and experimental validation," *IEEE Trans. Geosci. Remote Sens.*, vol. 48, no. 6, pp. 2740–2749, Jun. 2010.
[3] D. Gromek, K. Kulpa, and P. Samczynski, "Experimental results of passive SAR imaging using DVB-T illuminators of opportunity," *IEEE Geosci. Remote Sens. Lett.*, vol. 13, no. 8, pp. 1124–1128, Aug. 2016.
[4] R. Klemm, "Comparison between monostatic and bistatic antenna configurations for STAP," *IEEE Trans. Aerosp. Electron. Syst.*, vol. 36, no. 2, pp. 596–608, Apr. 2000.
[5] R. Nitzberg, "An effect of range-heterogeneous clutter on adaptive Doppler filters," *IEEE Trans. Aerosp. Electron. Syst.*, vol. 26, no. 3, pp. 475–480, May 1990.
[6] F. Colone, "Spectral slope-based approach for mitigating bistatic space-time adaptive processing clutter dispersion," *IET Radar, Sonar Navigat.*, vol. 5, no. 5, pp. 593–603, 2011.
[7] K. Duman and B. Yazici, "Moving target artifacts in bistatic synthetic aperture radar images," *IEEE Trans. Comput. Imaging*, vol. 1, no. 1, pp. 30–43, Mar. 2015.
[8] Z. Y. Li, "Research on bistatic SAR moving target detection and imaging technology," Ph.D. dissertation, School Electron. Eng., Beijing, China, 2017.
[9] J. Wan, Y. Zhou, L. Zhang, and Z. Chen, "Ground moving target focusing and motion parameter estimation method via MSOKT for synthetic aperture radar," *IET Signal Process.*, vol. 13, no. 5, pp. 528–537, Jul. 2019.
[10] Z. Li, J. Wu, Y. Huang, Z. Sun, and J. Yang, "Ground-moving target imaging and velocity estimation based on mismatched compression for bistatic forward-looking SAR," *IEEE Trans. Geosci. Remote Sens.*, vol. 54, no. 6, pp. 3277–3291, Jun. 2016.
[11] J. Wu, Z. Li, Y. Huang, J. Yang, H. Yang, and Q. H. Liu, "Focusing bistatic forward-looking sar with stationary transmitter based on keystone transform and nonlinear chirp scaling," *IEEE Geosci. Remote Sens. Lett.*, vol. 11, no. 1, pp. 148–152, Jan. 2014.
[12] F. Colone, D. Pastina, P. Falcone, and P. Lombardo, "WiFi-based passive ISAR for high-resolution cross-range profiling of moving targets," *IEEE Trans. Geosci. Remote Sens.*, vol. 52, no. 6, pp. 3486–3501, Jun. 2014.
[13] L. Wang and B. Yazici, "Bistatic synthetic aperture radar imaging of moving targets using ultra-narrowband continuous waveforms," *SIAM J. Imag. Sci.*, vol. 7, no. 2, pp. 824–866, Jan. 2014.
[14] D. Cerutti-Maori and I. Sikaneta, "A generalization of DPCA processing for multichannel SAR/GMTI radars," *IEEE Trans. Geosci. Remote Sens.*, vol. 51, no. 1, pp. 560–572, Jan. 2013.
[15] W. Melvin, "Space-time adaptive radar performance in heterogeneous clutter," *IEEE Trans. Aerosp. Electron. Syst.*, vol. 36, no. 2, pp. 621–633, Apr. 2000.
[16] C. Gierull, "Statistical analysis of multilook SAR interferograms for CFAR detection of ground moving targets," *IEEE Trans. Geosci. Remote Sens.*, vol. 42, no. 4, pp. 691–701, Apr. 2004.
[17] I. Stojanovic and W. C. Karl, "Imaging of moving targets with multi-static SAR using an overcomplete dictionary," *IEEE J. Sel. Top. Signal Process.*, vol. 4, no. 1, pp. 164–176, Feb. 2010.
[18] L. Yang, L. Zhao, G. Bi, and L. Zhang, "SAR ground moving target imaging algorithm based on parametric and dynamic sparse Bayesian learning," *IEEE Trans. Geosci. Remote Sens.*, vol. 54, no. 4, pp. 2254–2267, Apr. 2016.
[19] W. Melvin and M. Davis, "Adaptive cancellation method for geometry-induced nonstationary bistatic clutter environments," *IEEE Trans. Aerosp. Electron. Syst.*, vol. 43, no. 2, pp. 651–672, Apr. 2007.
[20] S. Gelli, A. Bacci, M. Martorella, and F. Berizzi, "Clutter suppression and high-resolution imaging of noncooperative ground targets for bistatic airborne radar," *IEEE Trans. Aerosp. Electron. Syst.*, vol. 54, no. 2, pp. 932–949, Apr. 2018.
[21] S. Kogon and M. Zatman, "Bistatic STAP for airborne radar," in *Proc. Adapt. Sens. Array Process. Workshop*, 2000, pp. 1–6.
[22] B. Himed, Y. Zhang, and A. Hajjari, "STAP with angle-Doppler compensation for bistatic airborne radars," in *Proc. IEEE Radar Conf.*, Jun. 2002, pp. 311–317.
[23] S. Wacks and B. Yazici, "Doppler-DPCA and Doppler-ATI: Novel SAR modalities for imaging of moving targets using ultra-narrowband waveforms," *IEEE Trans. Comput. Imag.*, vol. 4, no. 1, pp. 125–136, Mar. 2018.
[24] D. L. Donoho, "Compressed sensing," *IEEE Trans. Inf. Theory*, vol. 52, no. 4, pp. 1289–1305, Apr. 2006.
[25] E. Candes, J. Romberg, and T. Tao, "Robust uncertainty principles: Exact signal reconstruction from highly incomplete frequency information," *IEEE Trans. Inf. Theory*, vol. 52, no. 2, pp. 489–509, Feb. 2006.
[26] V. M. Patel, G. R. Easley, D. M. Healy, Jr., and R. Chellappa, "Compressed synthetic aperture radar," *IEEE J. Sel. Topics Signal Process.*, vol. 4, no. 2, pp. 244–254, Apr. 2010.
[27] X. Quan, B. Guo, Y. Lu, B. Zhang, and Y. Wu, "Comparison of several sparse reconstruction algorithms in SAR imaging," in *Proc. IET Int. Radar Conf.*, 2015.
[28] N. Ö. Onhon and M. Cetin, "A sparsity-driven approach for joint SAR imaging and phase error correction," *IEEE Trans. Image Process.*, vol. 21, no. 4, pp. 2075–2088, Apr. 2012.
[29] M. Cetin and W. Karl, "Feature-enhanced synthetic aperture radar image formation based on nonquadratic regularization," *IEEE Trans. Image Process.*, vol. 10, no. 4, pp. 623–631, Apr. 2001.
[30] Z. Li, F. Santi, D. Pastina, and P. Lombardo, "Multi-frame fractional Fourier transform technique for moving target detection with space-based passive radar," *IET Radar, Sonar Navigat.*, vol. 11, no. 5, pp. 822–828, May 2017.
[31] S. Barbarossa, "Doppler-rate filtering for detecting moving targets with synthetic aperture radars," *Proc. SPIE*, vol. 1101, pp. 140–147, Aug. 1989.
[32] J. D. Blanchard, J. Tanner, and K. Wei, "Conjugate gradient iterative hard thresholding: Observed noise stability for compressed sensing," *IEEE Trans. Signal Process.*, vol. 63, no. 2, pp. 528–537, Jan. 2015.
[33] D. Li, M. Zhan, H. Liu, Y. Liao, and G. Liao, "A robust translational motion compensation method for ISAR imaging based on keystone transform and fractional Fourier transform under low SNR environment," *IEEE Trans. Aerosp. Electron. Syst.*, vol. 53, no. 5, pp. 2140–2156, Oct. 2017.
[34] L. Mei, Z. Shuqing, and L. Chenlei, "Joint space-time–frequency method based on fractional Fourier transform to estimate moving target parameters for multistatic synthetic aperture radar," *IET Signal Process.*, vol. 7, no. 1, pp. 71–80, Feb. 2013.

XIN WANG (Member, IEEE) received the B.S. degree in electronic information engineering from the Nanjing University of Information Science and Technology, Nanjing, China, in 2006, and the Ph.D. degree in communication engineering from the Nanjing University of Aeronautics and Astronautics, Nanjing, in 2011.

From 2011 to 2015, she was an Assistant Professor with the Department of Communication Engineering, College of Telecommunication and Information Engineering, Nanjing University of Posts and Telecommunications, Nanjing, where she is currently an Associate Professor. Her research interests include the synthetic aperture radar imaging and signal processing, deep learning-based inverse imaging, and moving target refocusing.

XIAOZONG SONG received the B.S. degree in communication engineering from Shandong Agricultural University, Taian, China, in 2019. She is currently pursuing the M.S. degree with the Department of Communication Engineering, College of Telecommunication and Information Engineering, Nanjing University of Posts and Telecommunications, Nanjing, China.

Her current research interest is the super-resolution reconstruction of synthetic aperture radar.